Polymer Degradation and Stability 154 (2018) 222–233

Contents lists available at ScienceDirect

Polymer Degradation and Stability

journal homepage: www.elsevier.com/locate/polydegstab

# Situ preparation of $SiO_2$ on graphene-assisted anti-oxidation for resol phenolic resin

You Lv [a], Jian Li [b], Zixuan Lei [a], Ziqi Li [a], Xinli Jing [c], Yuhong Liu [a, *]

[a] Department of Chemical Engineering, School of Chemical Engineering and Technology, Xi'an Jiaotong University, Xi'an, 710049, Shaanxi, China
[b] Xi'an Aerospace Composite Materials Research Institute, Xi'an, 710025, Shaanxi, China
[c] Department of Applied Chemistry, School of Science, Xi'an Jiaotong University, Xi'an, 710049, Shaanxi, China

ARTICLE INFO

*Article history:*
Received 17 February 2018
Received in revised form
25 May 2018
Accepted 12 June 2018
Available online 13 June 2018

*Keywords:*
Silica
Graphene
Phenolic resin
Oxidation resistance
Decomposition mechanism

ABSTRACT

Easily oxidized group of traditional phenolic resin (PF) results in poor oxidation resistance at high temperature, which is unable to satisfy the requirements of advanced aerospace vehicles for high-performance application, especially ablation resistance. In order to improve the oxidation resistance of PF, a $SiO_2$/RGO binary hybrid nanomaterial assisted anti-oxidation for PF was designed. Here, we reported a simple sol-gel process and high temperature reduction for synthesis of dispersed $SiO_2$ nanoparticles on graphene (G-S). The designed structure of G-S was confirmed by FTIR, XRD, SEM and TEM. Introduction of G-S into PF (P-G-S) was beneficial to enhancement of oxidation resistance in whole temperature range (0–1000 °C). P-G-S-3 (3 wt.% of G-S) exhibits both lower thermal oxidative decomposition rate and higher termination temperature of thermal oxidative decomposition (increase from about 750 °C up to 900 °C) than those of neat PF in air. In addition, P-G-S-3 decomposed by thermal oxidation in air (at 557 °C, weight loss> 30 wt.%) later than neat PF (at 519 °C, weight loss> 20 wt.%). What's more, compared to the collapse of skeleton structure and few residual fragments of neat PF, P-G-S-3 showed greater oxidation resistance which resulted in the retention of a large number of aromatic C-C, methylene and different kinds of ether bond at temperature from 550 °C to 700 °C by FTIR and XPS. The section of P-G-S-3 expresses skin lamination that can act as a barrier to slow down the diffusion of oxygen into resin matrix. And $SiO_2$ on the surface protected the matrix continually as indicated from the SEM analysis.



## 1. Introduction

PF is the resin matrix with excellent mechanical and thermal performances which is the earliest and still widely used at present in many industries, especially in aerospace field. Recent decades, much effort has been made to improve thermal stability and char yield of PF in inert atmosphere by introducing inorganic elements or structure modification of molecular chains, such as titanium [1,2], boron [3–5], silicon [6,7], zirconium [8]. Also, oxidation resistance of PF due to easily oxidized group needs to be further improved for the applications in ablative and refractory materials. Shan Li and Tong Zhao et al. [9] presented the structure of silicone phenolic resin synthesized via esterification reaction and then controlled the degree of situ self-polymerization. The anti-oxidation properties of the silicone phenolic resin was improved due to silane groups grafted on the phenolic hydroxyl groups, which protected phenol groups from oxidation as well as resulted in the higher oxidation resistance by self-polymerized into silicone-rich domains. Zirconium diboride ($ZrB_2$) is an ultra-high temperature ceramic material with good oxidation and chemical attack resistance. The tests of ablation reveal that $ZrB_2$ is decomposed into zirconia ($ZrO_2$) and boria ($B_2O_3$) at high temperatures and it can hinder the oxygen transportation [10].

For thermal protection materials, it is intended to withstand exposure to all extreme environments which cause a series of physical and chemical changes on the surface or interior of the material. Especially, under the high temperature condition and oxidative atmosphere, pyrolysis, oxidation and oxidative decomposition occur simultaneously in different parts of materials. Thus, compared to explorations in inert atmosphere, it is also significant to research anti-oxidation properties of PF in oxidative atmosphere at high temperature. Char yield is one of the important parameters

* Corresponding author.
*E-mail address:* liuyuh@xjtu.edu.cn (Y. Liu).

https://doi.org/10.1016/j.polymdegradstab.2018.06.008
0141-3910/

to exam the ablation resistance and structural integrity of composite [11]. But during the formation of char, a large number of micro-cracks and porous structure which are oxygen diffusion channels are formed and extend from surface to the interior of materials resulting from thermal oxidative decomposition. This phenomenon will reduce the char yield and destroy integrated structure of composite, resulting in the failure of thermal protection.

Fortunately, with the discovery of graphene (GR) [12] and carbon nanotubes (CNT) [13,14], a new direction is proposed for improving thermal stability [15,16], mechanical property [17–22] and thermal conductivity [23,24] of matrix material due to the attractive integrated properties of GR and CNT.

What's more, GR has been introduce into inorganic and organic material for enhancing the oxidation resistance. Yitao Xu, Ying Guo and Xianzhu Fu et al. [25] synthesized a copper spherical particles encapsulated in reduced graphene oxide (RGO) nano-sheets (Cu@RGO) through a simple electrostatic self-assembly process followed by chemical reduction. The oxidation resistance of modified Cu was remarkably enhanced. Consequently, there are no sign of oxidation in air after storage at room temperature for 70 days and heat treatment at 130 °C for 1.5 h respectively. Furthermore, it has been reported that the layered materials is thought to be the formation of protective barrier during combustion [26]. Dongwoo [27] draw the same conclusion that the physical barrier effect of GR plays a pivotal role to protect Fe and Cu from oxidation through layer-by-layer assembly fabricated and transferred to Fe and Cu foils. And Chenlu [28] presented a functionalized GO modified polystyrene (FGO-P). The fire safety properties of the composite are improved, including the peak CO release rate (66% decrease), peak $CO_2$ release rate (54% decrease) and thermal degradation rate (30% decrease) et al. because of physical barrier effect of GO. In above studies, the physical barrier effect of GR slows down the diffusion of gases and degradation products. However, GR tends to combustion due to its weak thermal-oxidative stability, which destroys its unique layered structure affecting its physical barrier effect. Also, the thermal stability of GR in an oxygen-rich atmosphere is worse than that in an inert atmosphere. Therefore, if GR is isolated from oxygen at elevated temperatures by surface modification, it will be an effective measure to protect and give full play to retard the diffusion of gases. To achieve this target, in this work, we report a simple sol-gel process for synthesis of dispersed $SiO_2$ nanoparticles on GR with the aim to protect and improve the oxidation resistance of GR.

In this case, GO modified with (3-aminopropyl) triethoxysilane (MGO), then co-sol-gel design of tetraethyl orthosilicate (TEOS) and (3-aminopropyl) triethoxysilane (APTES) was carried out in the presence of MGO to introduce silica onto GO (MGO-$SiO_2$). Finally, G-S was obtained by calcination of MGO-$SiO_2$ at 600 °C in $N_2$ for 2 h to removal of unsaturated hydroxyl groups on the surface of silica and reduction of GO. The thermal stability and oxidation resistance of P-G-S was studied by TG analysis and high-temperature oxidation test. The structural changes for neat PF and P-G-S-3 during decomposition at different temperatures interval and atmosphere was discussed.

## 2. Experimental

### 2.1. Chemicals

Resol type PF resin (a solid content of 70 ± 3 wt.%, ethanol as solvent) was supplied by DeQing TianCheng Colophony Co. Ltd, China. Flake graphite, concentrated $H_2SO_4$, concentrated ammonia solution (28–30%), concentrated hydrochloric acid, $KMnO_4$, $NaNO_3$ and ethanol were purchased by Sinopharm Chemical Reagent Co. Ltd. (3-aminopropyl) Triethoxysilane (APTES), dicyclohexylcarbodiimide (DCC), tetraethylorthosilicate (TEOS) were obtained from Shanghai Macklin Biochemical Co. Ltd. Deionized water was used for all experiments.

### 2.2. Synthesis of GO

GO was synthesized from graphite via a modified Hummers method [29]. Accordingly, commercial graphite (5.0 g) and $NaNO_3$ (2.5 g) were added into a solution of concentrated $H_2SO_4$ (115 mL) with ice-water bath. Subsequently, $KMnO_4$ (15 g) was slowly added into the mixture. The solution was keeping stirring at 0 °C for 2 h, and then at 35 °C for 2–4 h. Then, deionized water was very slowly added to the flask until temperature of system did not continue to rise. Then, the solution was further stirred for 15 min at 98 °C and a lot of deionized water as well as 50 mL $H_2O_2$ were added to stop reaction. After that, the suspension was washed twice with 5% HCl solution and three times with distilled water and then dialyzed for a week. Finally, the GO was obtained by centrifuged and then freeze-drying.

### 2.3. Synthesis of (3-aminopropyl) triethoxysilane-modified GO (MGO)

GO (0.1 g) was dispersed in ethanol (100 mL) via ultrasonication for 1 h to achieve a homogeneous mixture. Then DCC (50 mg) and APTES in ethanol (1.6 g in 30 mL) were slowly dripped into GO dispersions and stirring was continued at 75 °C for 12 h in nitrogen atmosphere. Then the product was washed with ethanol twice and drying in vacuum at 60 °C for 24 h.

### 2.4. Synthesis of the $SiO_2$ nanoparticles on GR sheets (G-S)

The MGO-$SiO_2$ sheets were prepared via co-sol-gel design approach of TEOS and APTES on MGO. In detail, MGO was dispersed in ethanol and sonicated in cell crushing apparatus for 1 h with a concentration of ~1.0 mg/mL. In the sol-gel process, a small amount of concentrated ammonia solution (0.05 mL) was added into GO ethanol suspension. After stirring for 30 min, 1.00 g of TEOS was slowly dripped into the above solution. And the mixture was kept stirring at room temperature for 24 h to form amorphous silica nanoparticles on the GO sheets. The product was washed with ethanol and drying in vacuum at 60 °C for 24 h. In the second thermal treatment procedure, G-S was obtained by calcining at 600 °C in $N_2$ for 2 h to removal of unsaturated hydroxyl groups on the surface of silica and reduction of GO.

### 2.5. Preparation of the G-S modified PF (P-G-S) and curing process

The moderate G-S-X powder was dispersed in ethanol via ultrasonication using ultrasonic cell crusher for 30 min to reduce aggregation. The blend specimens (P-G-S-X, X represents wt.%) were prepared by mixing resol resin and ethanol dispersions of G-S under stirring for 1 h, then removing excess solvent via vacuum distillation. Finally, P-G-S-X and neat PF were cured at 125 °C for 1 h, 145 °C for 2 h, 175 °C for 4 h and 200 °C for 1 h according to Differential Scanning Calorimetry (DSC) analysis.

### 2.6. Characterization

Two types of cured resin were heat-treated to 240 °C, 375 °C, 530 °C, 700 °C under nitrogen atmosphere and 375 °C, 475 °C, 550 °C, 700 °C under oxidative atmosphere according to DTG curves, then the residues heat treated under different temperatures were analyzed using Fourier Transform Infrared Spectroscopy

(FTIR) and X-ray Photoelectron Spectroscopy (XPS). The FTIR measurements were carried out using a ReactIRIC10 spectra of Meteler Toledo at a 4 $cm^{-1}$ resolution in the range of 400–4000 $cm^{-1}$. Samples were grinded, mixed with KBr and pressed into small flakes for testing. The X-ray Photoelectron Spectroscopy (XPS) measurement was performed using an ESCALAB250XI instrument. X-ray Diffraction (XRD) pattern were collected on a Bruker D8 diffractometer with Cu Kα radiation (λ = 0.1540 nm) at an accelerating voltage of 35 kV and a current of 20 mA. Samples were scanned from 0.3 to 40° at the step scan mode. The morphology of the GR, GO, G-S, neat PF and P-G-S-3 was characterized with Transmission Electron Microscopy (TEM) on a TECNAI G2 spirit BioTwin operated at 200 kV and Scanning Electron Microscope (SEM) on a Hitachi S-4800 equipped with Energy Dispersive X-Ray spectrometer (EDX). Thermal and oxidative stability of the P-G-S were investigated with Thermogravimetric Analysis (TGA) using a Netzsch STA409PC at a temperature scan rate of 10 °C/min in a 30–1000 °C temperature range under air and nitrogen atmosphere at a flow rate of 50 mL/min.

## 3. Results and discussion

### 3.1. Characterization of GO, MGO and G-S

The structure and morphology of GO and G-S are investigated by SEM and TEM. SEM images of GO and G-S were show in Fig. 1a and b. According to the image of 1a, two dimensional smooth sheet-like layers structure of GO can be seen clearly, and also with the appearance of wrinkles on the surface resulting from different interaction forces among oxidized functional groups. But G-S expressed as a rough sheet because of the reduction and the coating of $SiO_2$ (Fig. 1b). Then, the presence of C, O and Si elements of G-S is also confirmed by EDX spectrum (Fig. 2a–c). As shown from Si mapping (Fig. 2c), bright dots corresponding to Si atoms homogeneously distribute, reflecting that dense nanosilica uniformly covers on GR sheets without any obvious vacancies. In addition, TEM image (Fig. 1c) of GO also shows two-dimensional wrinkled and folding layer. TEM image (Fig. 1d) of G-S also shows typical single or overlapping sheet-like shape in G-S and reveals that a large number of $SiO_2$ nanoparticles with a diameter of about 10 nm are dispersed on GR sheets. Also, there is no apparent agglomeration of $SiO_2$ on GR. This is indicated that the agglomeration of $SiO_2$ nanoparticle and GO can be effectively prevented.

Fig. 3a shows XRD spectra of GO and MGO. Compared with characteristic diffraction peak of graphite at 2θ = 26° (002), the characteristic diffraction peak of GO is at 2θ Bragg angle of 11.3° corresponding to an interlayer space increasing from 0.34 to 0.76 nm. This is resulted from insertion of oxygenated functional groups between graphite sheets due to the oxidation process of graphite. After reaction with APTES, there are two peaks (Fig. 3a) at 5.78° and 9.55° corresponding interlayer spacing is 1.53 nm and 0.93 nm, respectively. From the result, the interlayer space of GO expands from 0.76 nm to 1.53 nm is due to the APTES is completely inserted into the interlayer of GO, and incomplete intercalation of APTES results in the interlayer space only increases to 0.93 nm. Moreover, the Small-angle XRD is used to characterize the G-S material. According to the result of Fig. 4a, there is no diffraction peak in the range of 0~5°. This is due to there is no formation of ordered mesoporous structure of $SiO_2$ after calcination at 600 °C for 2 h. Also, the originally ordered interlayer structure of GO becomes disorder due to high temperature reduction. The result of Wide-angle XRD of G-S is shown in Fig. 4b, there is broad peak at the range from 20 to 25° which corresponds to the amorphous $SiO_2$. This indicates that there is no formation of ordered crystal structure of $SiO_2$ after calcination at 600 °C for 2 h. What's more important is that there are no diffraction peaks corresponding to GO, modified GOs and the restacking of graphene to form graphite can be observed, suggesting that the agglomeration of graphene sheets during the reduction process can be effectively prevented and a good dispersion of graphene coated by $SiO_2$ without overlap.

FTIR spectra of G, GO, MGO, MGO-$SiO_2$ and G-S are shown in Fig. 3b. Typical adsorption peaks of GO appear at wave number of 1626 $cm^{-1}$ (C-C in aromatic ring), 1725 $cm^{-1}$ (C=O carboxyl stretching vibration), 1261 $cm^{-1}$ (C-OH stretching vibration), 1052

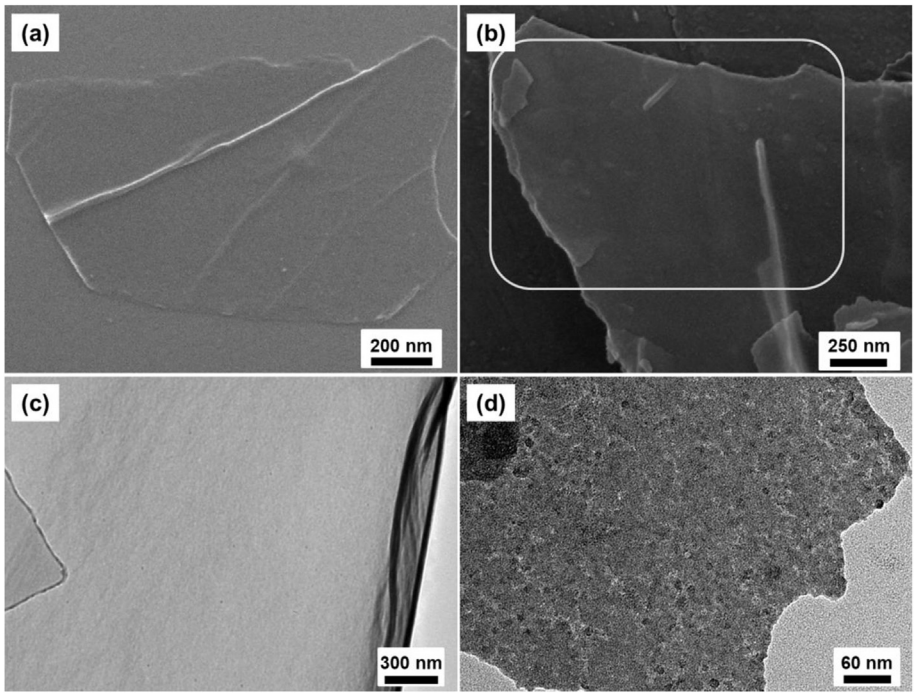


**Fig. 1.** SEM images of (a) GO and (b) G-S (The rectangular box is the scan section of EDX); TEM images of (c) GO and (d) G-S.

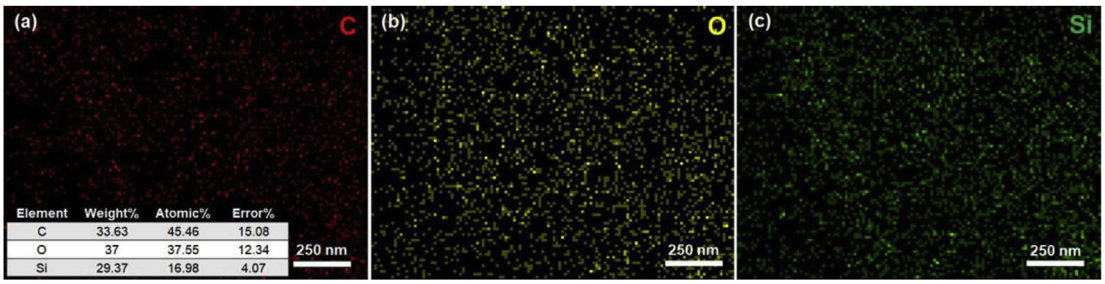


**Fig. 2.** EDX element maps for (a) C; (b) O and (c) Si of G-S in SEM images (Fig. 1b).

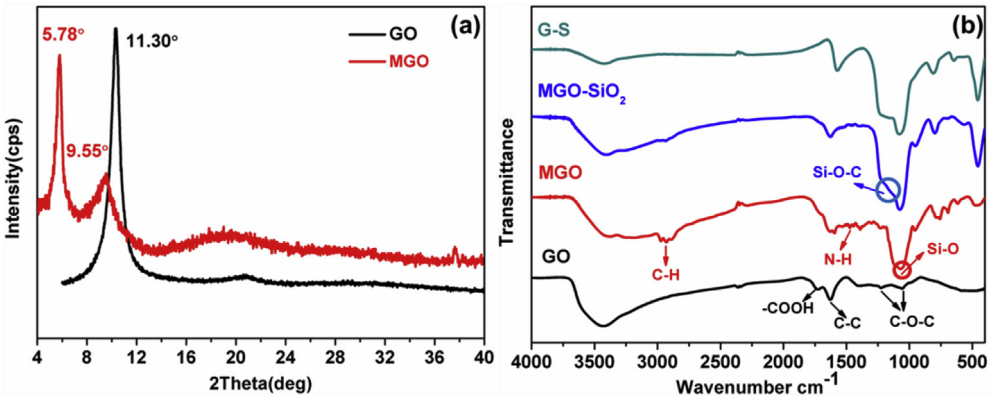


**Fig. 3.** (A) XRD pattern of GO and MGO; (b) FTIR spectra for GO, MGO, MGO-$SiO_2$ and G-S.

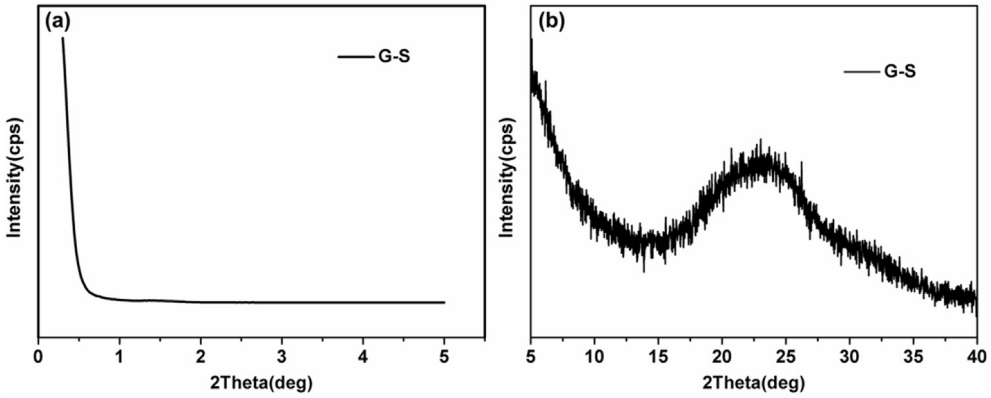


**Fig. 4.** XRD patterns of G-S: (a) Small-angle; (b) Wide-angle.

and 805 $cm^{-1}$ (C-O vibration of epoxide groups) and the broad peak at 3000–3500 $cm^{-1}$ is attributed to the stretching vibration of hydroxyl groups (-OH). Additionally, there are some new appearance of intense bands in region of 2800–3000 $cm^{-1}$ for MGO and MGO-$SiO_2$, which is assigned to alkyl chain (C-H) from APTES. And the peak at 1572 $cm^{-1}$ (N-H stretching vibration) confirms the opening reaction resulting in –C-NH-C- between the epoxide groups and the amine groups. Furthermore, appearance of the peaks at 1208 $cm^{-1}$ (Si-O-C symmetric stretching), 1097 $cm^{-1}$ (Si-O-Si asymmetric vibration), 958 $cm^{-1}$ (Si-OH bending vibration), 800 $cm^{-1}$ (Si-O stretching vibration) and 467 $cm^{-1}$ (Si-O bending vibration) provide valid evidence for the successful synthesis of MGO and MGO-$SiO_2$. After calcining, typical alkyl chain peaks at 2800–3000 $cm^{-1}$ and Si-OH bending vibration peak at 958 $cm^{-1}$ disappear. Meanwhile the peaks of C-C bond and silicon functional groups of G-S become more obvious. Altogether, the residual hydroxyl groups on the surface of G-S have been completely reacted and alkyl chains have been removed.

### *3.2. Thermal oxidative decomposition mechanism for two types of resin at different temperature range*

#### *3.2.1. Oxidation resistance and structure of two cured resin*

In order to investigate oxidation resistance for two types of resin at different temperature intervals, TG analysis is carried out in inert and oxidative atmosphere firstly. And the results of two curves (TG and DTG) are shown in Fig. 6 respectively. According to the results of Fig. 6b, compared to neat PF, the residue and termination temperature of oxidative decomposition are increased with an increase of introduced amount of G-S in air. And the most obvious

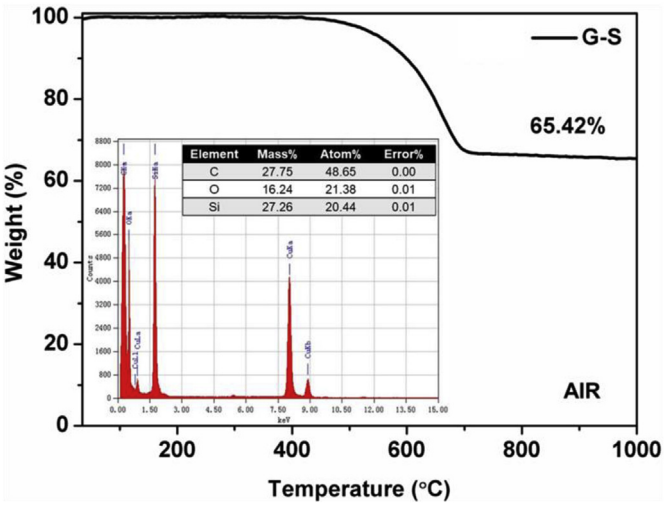


**Fig. 5.** TGA curve and the elements content of G-S by EDX attached to TEM (Fig. 1d).

improvement is occurred in presence of 3 wt.% of G-S. However, the char yield decreased to the lowest level in inert atmosphere (as shown in Fig. 6a). This phenomenon may be attributed to too much modifier that reduces crosslink density of P-G-S-3. In order to compare the effects of different structures of nanomaterial on property, $SiO_2$ and RGO are introduced into resol resin (P-RGO-$SiO_2$) separately. And relative content of each material of G-S is confirmed by TG in air (Fig. 5) which is consistent with the result of EDX attached to TEM. The oxidation resistance of P-RGO-$SiO_2$ is the worst of the three types of resin, which may result from extreme decline of crosslink because of too large volume fraction of single GR and $SiO_2$ system. This result indicates that different structure of the same materials express difference physical state and chemical properties. Thus, G-S modified PF with content of 3 wt.% (P-G-S-3) is considered to be the most appropriate candidate in the following study.

The whole decomposition of neat PF and P-G-S-3 can be interpret from Scheme 1 and divided into two regions in air. First of all, the initial stage is corresponding temperature range in RT~519 °C for neat PF and RT~489.7 °C for P-G-S-3. The weight loss of both resin (about 20 wt.%) is basically the same as they are in $N_2$ atmosphere (listed in Table 1). It can be analyzed by the same mechanism as inert atmosphere. Then, a large number of pores are produced on surface and inside of resin with the increase of temperature, which provides oxygen diffusion channels. The thermal oxidative decomposition takes place of pyrolysis becoming dominant reaction. And corresponding starting temperature at this stage is about 519 °C for neat PF and 557 °C for P-G-S-3. This is indicated that the oxidation resistance of P-G-S-3 is better than of that of neat PF. The introduction of G-S can slow down the diffusion rate of $O_2$, which is due to graphene-like structure of G-S and $SiO_2$ coating on surface. This special structure is an effective method to improve the oxidation resistance of G-S. Thus, at such high temperature, G-S can still play a role that is preventing and slow down the diffusion rate of oxygen in whole process.

The core-level XPS measurement is performed to identify the elements on surface of P-G-S-3 and neat PF determining chemical states and binding characteristics. Fig. 7b–f shows carbon, oxygen and silicon peaks detected from the full-scan XPS spectrum of P-G-S-3 and neat PF.

Fig. 7b and e represent a high-resolution C 1s XPS spectrum for both types resin and the asymmetric shape of C 1s peak at 284.8 ± 0.1 eV indicates existence of different components. The C 1s spectra of binding energies were deconvoluted by Lorentzian-Gaussian fitting into four peaks and three peaks respectively. Fig. 7e corresponding P-G-S-3 shows three peaks at 284.8 ± 0.1 eV, 285.9 ± 0.1 eV and 286.7 ± 0.1 eV that correspond to un-oxidized graphite carbon skeleton (C-C), ether bond (C-O-C) and hydroxyl group (C-OH) respectively. However, Fig. 7b corresponding neat PF

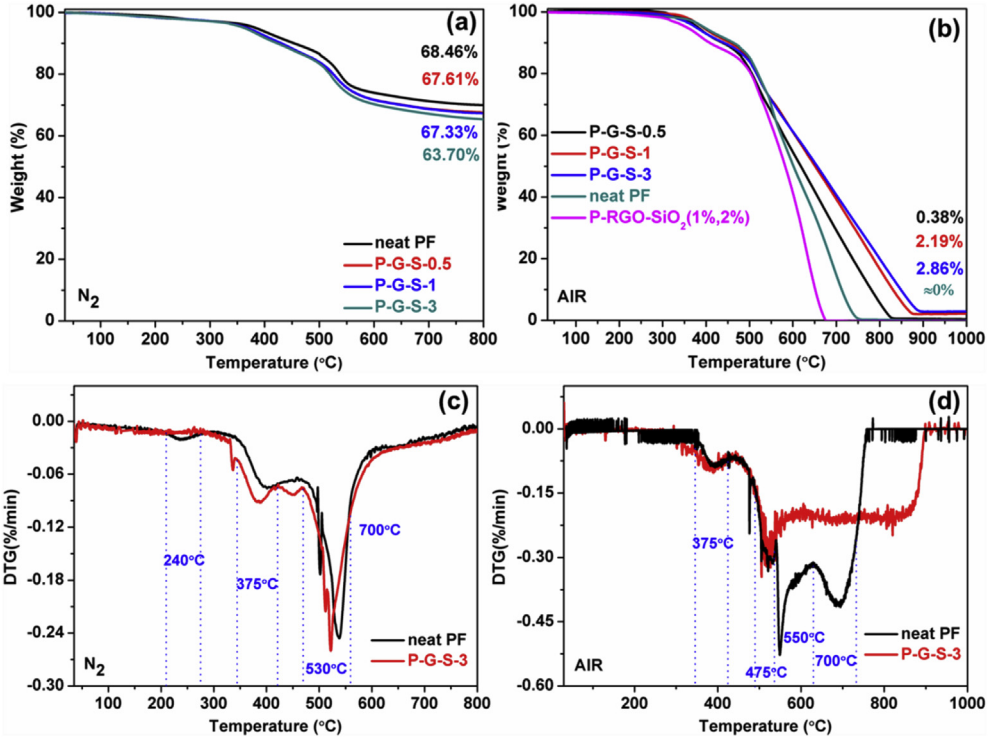


**Fig. 6.** TGA curves of neat PF, G-S and P-G-S with different amount of G-S: (a) (b); (c) (d) DTG curves of neat PF and P-G-S-3.

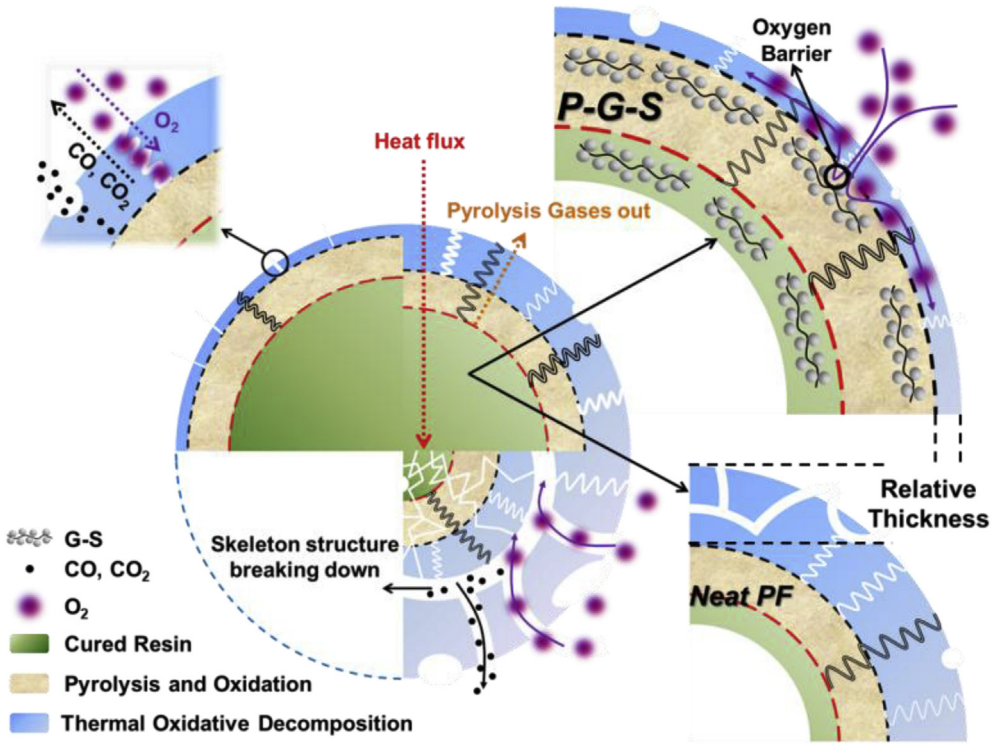


**Scheme 1.** Thermal oxidative decomposition process of neat PF and P-G-S-3 in air (relative thickness represents the intensity of the corresponding reaction process).

**Table 1**
Weight loss of neat PF and P-G-S-3 during decomposition in different atmosphere and temperature.

| Neat PF | | | P-G-S-3 | | |
|---|---|---|---|---|---|
| T (°C) | Weight loss in air (%) | Weight loss in $N_2$ (%) | T (°C) | Weight loss in air (%) | Weight loss in $N_2$ (%) |
| 436.167 | 10 | 10.6 | 441.174 | 10 | 11.0 |
| 519.333 | 20 | 17.0 | 516.674 | 20 | 19.0 |
| 549.500 | 30 | 23.0 | 557.174 | 30 | 27.0 |
| 573.167 | 40 | 25.0 | 601.174 | 40 | 30.0 |
| 601.333 | 50 | 26.0 | 651.174 | 50 | 31.5 |
| 632.167 | 60 | 27.0 | 698.674 | 60 | 33.0 |
| 661.667 | 70 | 28.0 | 751.674 | 70 | 34.0 |
| 687.000 | 80 | 28.5 | 799.674 | 80 | 34.6 |
| 712.333 | 90 | 29.0 | 848.674 | 90 | 35.0 |
| 764.000 | 100 | 30.0 | 901.174 | 100 | 35.3 |

shows four chemical states, and extra peak at 287.3 ± 0.1 eV that correspond to carboxyl group (C═O). This is resulting from methylene group (-$CH_2$-) is oxidized to benzophenone (C═O) with presence of air and water in curing environment [30]. Oxidation process is shown in reaction (1) of Scheme 2. It is can be indicated that P-G-S-3 has better oxidation resistance than that of neat PF in curing process. And this difference is not obvious in the FTIR spectra (Fig. 8). Also, Table 2 shows the area percentages of C-O-C bonds (285.9 eV) are 11.7% in P-G-S-3 and 23.3% in neat PF, which indicates that the reaction of P-G-S-3 produced more methylene groups and less ether bonding. The stability of ether linkage is poor, and it is liable to be decomposed in oxidative atmosphere. Therefore, adding G-S increased content of methylene group and oxidation resistance in P-G-S-3. And percentages of C-C bonds (284.8 eV) were 80% in P-G-S-3 and 68.8% in neat PF.

The core-level spectra of O 1s (Fig. 7c, f) shows two same peaks of C-O-C and C-OH located at 533.3 and 532.6 eV respectively. The peak at 531.6 ± 0.1 eV (C═O) in neat PF results from same reason in oxidation. And extra peak (O-Si) at 532.9 ± 0.1 eV (O-Si) in P-G-S-3 is due to the presence of G-S. High resolution Si 2p peak is separated, and signals at 103.2 eV and 102.4 eV, corresponding to $SiO_2$ and Si-O structures respectively.

### 3.2.2. *Pyrolysis process of P-G-S-3 and neat PF in inert atmosphere*

The pyrolysis mechanism can be used as an assistant to explain the process of thermal oxidative decomposition. Thus, FTIR spectra of P-G-S-3 residues (heat treated to 0, 240, 375, 530 and 700 °C for 30 min) are confirmed from DTG curves which are shown in Fig. 6c, when compared with spectrum of neat PF. Following recognized peaks identification of infrared spectrum of functional groups corresponding to the major peaks of spectra have been identified as listed in Table 4.

When temperature increases to 375 °C, the disappearance of hydroxymethyl C-O peak (1010 $cm^{-1}$) and decrease of phenolic O-H peak intensity (1360 $cm^{-1}$) for all tested resin are result from post curing reaction [31]. Ether bond C-O peaks intensity from 1060 to 1300 $cm^{-1}$ increase (Fig. 8a and b) is a same mechanism. Possible processes are shown in reactions (1), (2), (3) and (4) of Scheme 2.

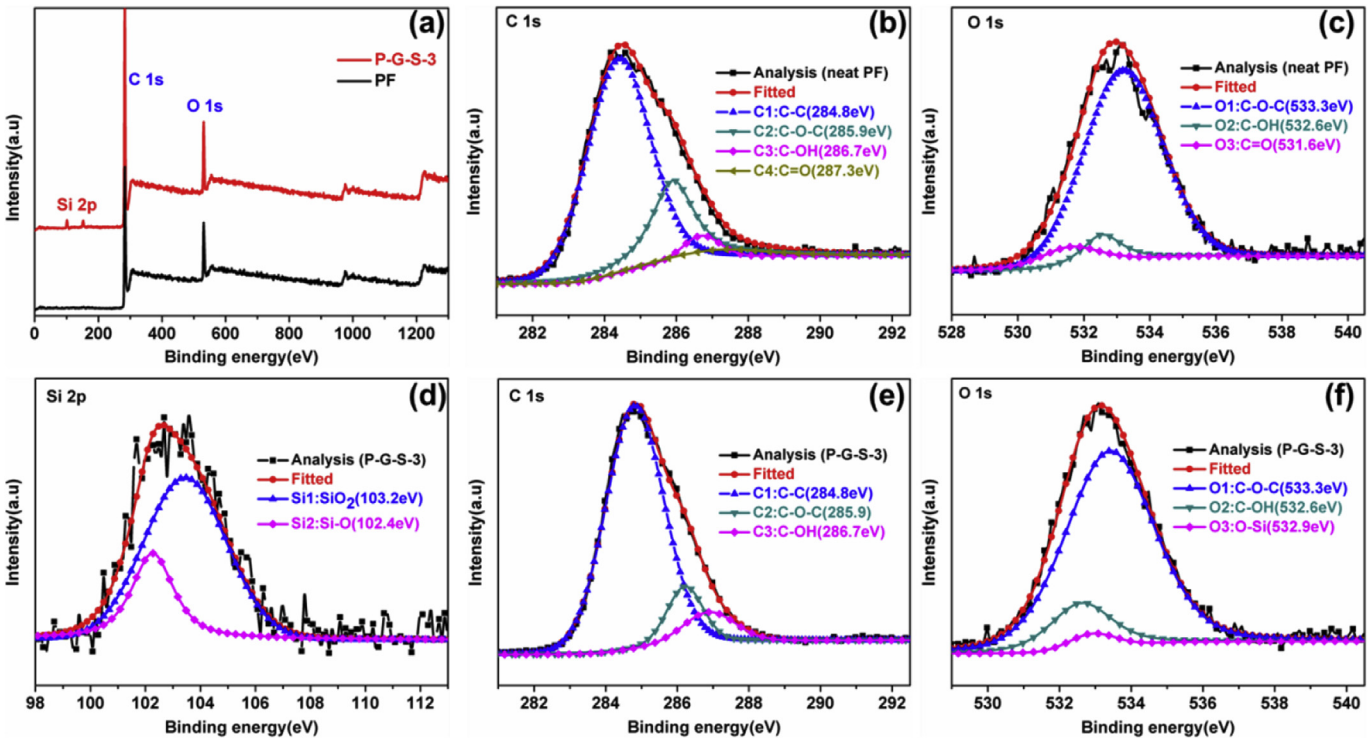


**Fig. 7.** X-ray photoelectron spectra of neat PF and P-G-S-3: (a) full scan, (b) (e) C 1s core-spectrum, (c) (f) O 1s core-spectrum, (d) high resolution Si 2p.

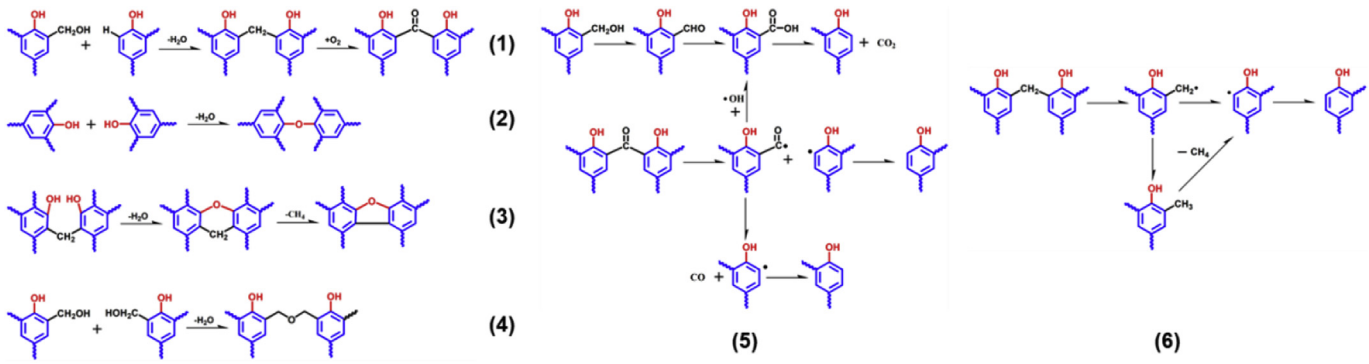


**Scheme 2.** Possible reactions of neat PF and P-G-S-3 at elevated temperature during pyrolysis and oxidation process.

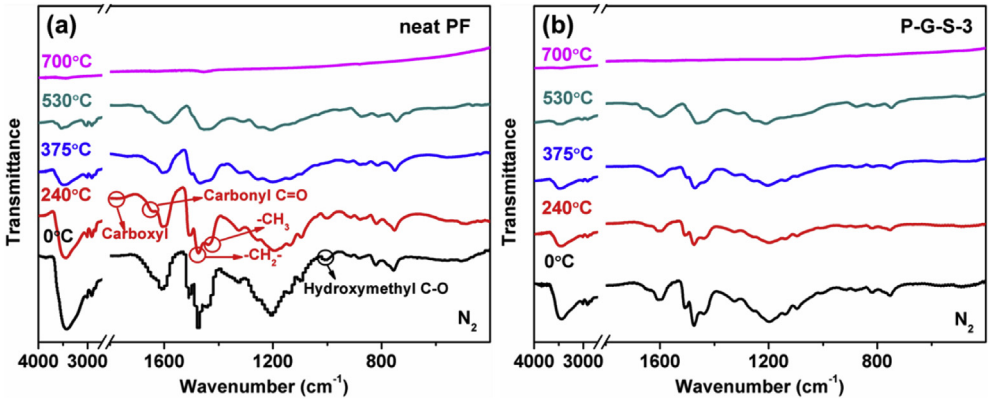


**Fig. 8.** FTIR spectra for two types of resin in $N_2$ during pyrolysis: (a) neat PF and (b) P-G-S-3.

**Table 2**
Area of Chemical bond species and corresponding binding energy of XPS spectra.

| Component | | Neat PF | | P-G-S-3 | |
|---|---|---|---|---|---|
| | Binding Energy (eV) | Area | Area (%) | Area | Area (%) |
| C-C | 284.8 | 17500.4 | 68.8 | 36079.2 | 80.0 |
| C-O-C | 285.9 | 5927.4 | 23.3 | 5282.2 | 11.7 |
| C-OH | 286.7 | 1000.4 | 3.9 | 3718.5 | 8.3 |
| C=O | 287.3 | 1000.0 | 3.9 | \ | \ |
| C-O-C | 533.3 | 8600.0 | 81.1 | 14000.0 | 82.3 |
| C-OH | 532.6 | 1000.0 | 9.4 | 2500.0 | 14.7 |
| C=O | 531.6 | 1000.0 | 9.4 | \ | \ |
| O-Si | 532.9 | \ | \ | 500.0 | 3.0 |
| $SiO_2$ | 103.2 | \ | \ | 1282.9 | 73.4 |
| Si-O | 102.4 | \ | \ | 465.2 | 26.6 |

Thus, weight loss (about 5%) is due to the elimination of water and residual low molecular fragments in initial stage (up to 375 °C). What's more, it is remarkable that products are observed from extended oxidation path in addition to those from pyrolysis at this low temperature stage. For example, weak carboxylic band at 1740 $cm^{-1}$ and obvious carbonyl band at 1680 $cm^{-1}$ (Fig. 8a and b) appear in both resin (process shown in reaction 1and 5).

The maximum weight loss is at temperature from 375 to 530 °C, which is 13.76% of neat PF and 16.58% of P-G-S-3 (in Table 3). In this stage for all resin, crosslink structure begins to degradation. It is clearly shown (Fig. 8a and b) that remarkable decrease of intensity for methylene peak (1480 $cm^{-1}$) and transformation to methyl (1437 $cm^{-1}$) (in Scheme 2, reaction 6). And increasing intensity of peak at 1680 $cm^{-1}$ corresponding to carbonyl is due to continuous oxidation. Relative reactions are shown in reactions (1) in Scheme 2. In addition, it can be clearly seen that aliphatic ether structure (1060 $cm^{-1}$) almost disappears and few residual hydroxyl-substituted in phenol ring, biphenyl ether, xanthene and diphenylene oxide type inner-ring oxygen are remained at 530 °C.

Finally, two flat curves (Fig. 8a and b) at the temperature of 700 °C (loss in weight is about 10%) are showing respectively. It can be illustrated that phenolic hydroxyl, diphenyl ether and inner-ring oxygen products are decomposed completely and only remain residue of char.

As a result, there is a same pyrolysis mechanism for two types of resin at different temperature interval in nitrogen, which presents the same thermal stability and structural change accompanied by partial oxidation.

### 3.2.3. *Thermal oxidative decomposition process of P-G-S-3 and neat PF in air*

As for oxidative atmosphere, the special structure of G-S may play a role of anti-oxidation for resin. The process of decomposition for two systems is shown in Scheme 1. According to four peaks in DTG curves (as shown in Fig. 6d), powdered samples of both resin are treated at 375, 475, 550, 700 °C for 10min respectively using tube furnace in air. And structural change of neat PF and P-G-S-3 are characterized by FTIR and XPS analysis.

**Table 4**
Infrared bands and assignments for P-G-S-3 and neat PF.

| Wavenumbers ($cm^{-1}$) | Assignments |
|---|---|
| 3300 | O-H stretch |
| 3300–3100 | Aromatic C-H stretch |
| 2950–2800 | Aliphatic C-H stretch |
| 1740 | Carboxylic groups |
| 1680–1650 | Carbonyl C=O stretch |
| 1610, 1590, 1514 | Aromatic C-C stretch |
| 1480–1450 | $CH_2$ deformation |
| 1437 | Aliphatic $CH_3$ asymmetric bending |
| 1360, 1340 | Phenolic O-H in-plane deformation |
| 1300, 1280 | Xanthene C-O |
| 1260 | Biphenyl ether C-O stretch |
| 1220, 1160 | Alkyl-phenolic C-O stretch |
| 1196 | Diphenylene oxide C-O |
| 1095 | Si-O-Si asymmetric stretch |
| 1060 | Aliphatic ether C-O deformation |
| 1010 | Hydroxymethyl C-O deformation |
| 890–690 | Out-of-plane substituted rings C-H deformation |
| 798 | Si-O symmetric stretch |
| 466 | Si-O bending |

In initial stage, before at temperature of 375 °C, there are more obvious absorption peaks (Fig. 9a and b) of carboxylic (1740 $cm^{-1}$) and carbonyl (1650 $cm^{-1}$) due to oxidation. And the same weight loss (in Table 3) as in inert atmosphere shows it can be proposed the same mechanism at low temperature stage in different atmosphere.

From temperature at 375 °C–550 °C, compared with nitrogen atmosphere, the weight loss of PF is increased by 13% reaching 27%, but that of P-G-S-3 is only increased by 7% reaching 23% in air (as shown in Table 3). More loss in weight indicates thermal oxidative decomposition begins to occur at this stage. And neat PF are decomposed faster by thermal oxidation than P-G-S-3. Basing on the rate of oxidative decomposition increased with increasing oxygen concentration, we can conclude that there is more oxygen diffusing into the interior of the material. Furthermore, at this temperature range, chemical structures of two type of resin become very different from Fig. 9c. When temperature is up to 550 °C, the intensity of aromatic C-C peak (1600 $cm^{-1}$) for neat PF becomes weak. Also, it can be noticed that there are no ether bond as crosslink structure and merely remains apparent aliphatic -$CH_3$ (1437 $cm^{-1}$) and -$CH_2$ (1450 $cm^{-1}$). This phenomenon illustrates that ether bond is decomposed by thermal oxidative due to its poor anti-oxidation in presence of oxygen. On the contrary, for P-G-S-3, there is no obviously weakening intensity of C-C peak (Fig. 9c). It is worth noting that strong absorption peaks in the range of 1095–1300 $cm^{-1}$ including Si-O-Si (1095 $cm^{-1}$), biphenyl ether (1260 $cm^{-1}$), diphenylene oxide (1196 $cm^{-1}$) and xanthene (1300 $cm^{-1}$). In addition, XPS was also used to study the chemical states of carbon and silicon atoms in oxidized resin. The full scan spectrum is shown in Fig. 10, in which C, O, Si and Na are observed. And the reason of Na peak is due to NaOH as a catalyzer during the synthesis of PF. At the temperature of 550 °C, Fig. 11a and b show

**Table 3**
Weight loss of neat PF and P-G-S-3 during decomposition in different atmosphere and temperature range.

| Atmosphere | Resin type | Weight loss at different temperature range (%) | | | | Total weight loss |
|---|---|---|---|---|---|---|
| AIR | | RT~375 °C | 375–475 °C | 475–550 °C | 550–700 °C | RT~700 °C |
| | Neat PF | 3.32 | 7.71 | 19.22 | 55.01 | 85.25 |
| | P-G-S-3 | 4.76 | 7.92 | 15.74 | 30.84 | 59.26 |
| $N_2$ | | RT~240 °C | 240–375 °C | 375–530 °C | 530–700 °C | RT~700 °C |
| | Neat PF | 1.84 | 2.66 | 13.76 | 10.51 | 30.06 |
| | P-G-S-3 | 2.09 | 3.86 | 16.58 | 10.33 | 34.67 |

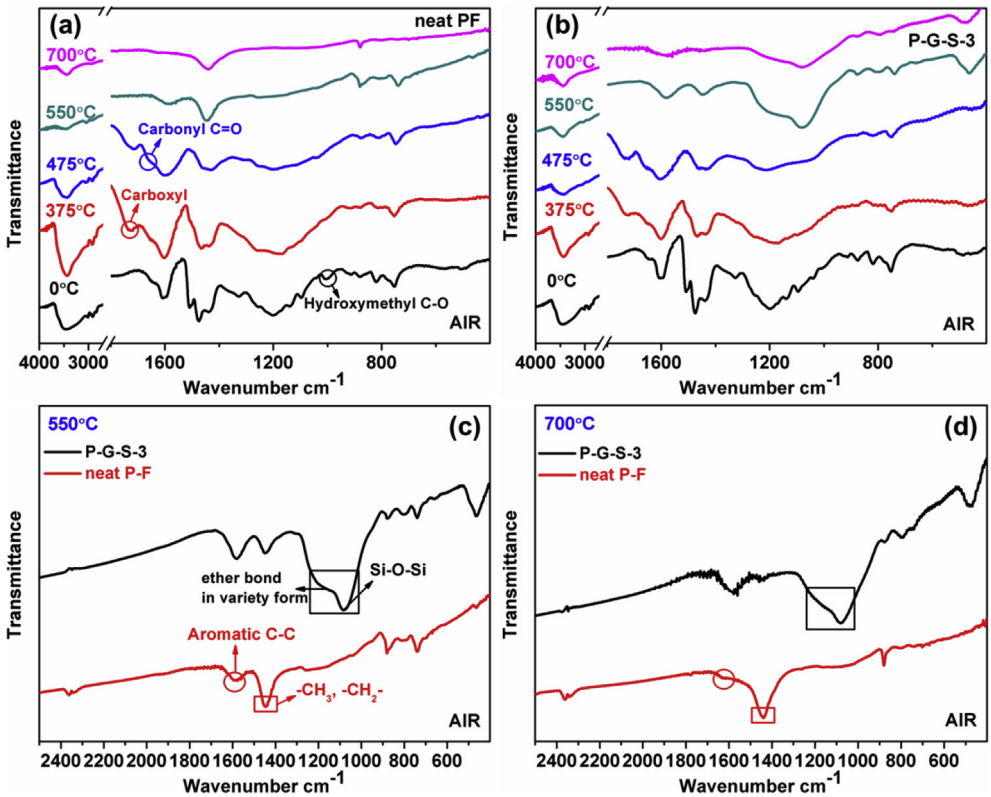


**Fig. 9.** FTIR spectra for two types of resin in air during thermal oxidative decomposition: (a) neat PF, (b) P-G-S-3; structural comparison at same temperature of: (c) 550 °C, (d) 700 °C.

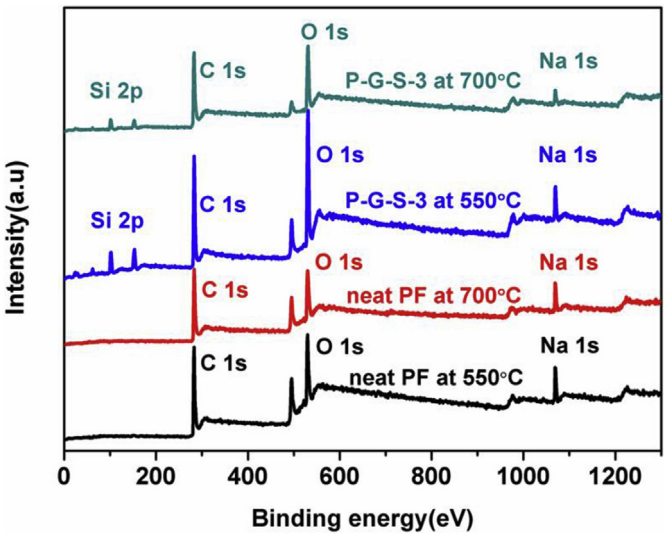


**Fig. 10.** Full scan of X-ray photoelectron spectra of neat PF and P-G-S-3 in air during thermal oxidative decomposition.

the area percentages of C-O-C bonds (285.9 eV) are 19.80% in P-G-S-3 and 5.28% in neat PF. This result is consistent with infrared (Fig. 9c), which indicates many kinds of forms of ether bond are remained for P-G-S-3 but not for neat PF. Also high resolution Si 2p is separated, and signals at 102.4 eV and 103.2, corresponding to Si-O and $SiO_2$ structures respectively in Fig. 11e.

At temperature from 550 °C to 700 °C, the inequality of thermal oxidative decomposition rate of both resin become more obvious. Neat PF is decomposed much faster than P-G-S-3, which can be concluded by the slope of TG and DTG curves (Fig. 6b and d). What's more, compared with nitrogen atmosphere, the weight loss of neat PF is increased by 45% reaching 55% and that of P-G-S-3 is merely increased by 20% reaching 33%. In addition, the residue of PF is null at temperature of 750 °C, but that of P-G-S remains about 37% at the same temperature (Table 3). Specific structure changes of both resin is analyzed by FTIR at this stage. When temperature is to 700 °C, aromatic C-C peak (1600 $cm^{-1}$) has disappeared and only remains aliphatic (1437 $cm^{-1}$) and methylene (1450 $cm^{-1}$) for neat PF in Fig. 9d. From this, it is inferred that the skeleton structure of neat PF has collapsed and only left fragments of the structure because of thermal oxidative decomposition. However, P-G-S-3 still remains aromatic C-C of skeleton structure, methylene and kinds of forms of ether bond (biphenyl, xanthene or diphenylene oxide type inner-ring oxygen) as crosslink points (Fig. 9d). In the same way, XPS was used to study the chemical states of the two resins treated at 700 °C (Fig. 11c and d). We can also draw the same conclusion as infrared analysis (Fig. 9d) as that P-G-S-3 still remains a large number of skeleton structure and ether crosslink. In addition, the area percentages of O-C═O bonds (288.4 eV) are 8.20% in P-G-S-3 and 14.55% in neat PF. It can be fully explained that the neat PF is more easily oxidized than P-G-S-3.

Surface morphology of two resin are also studied by SEM at different heat treatment temperature in air (as shown in Figs. 12 and 13). Firstly, the surface and section of neat PF are all smooth, but section of P-G-S-3 is rough due to introduction of G-S (Fig. 12a and b). After treated at 550 °C, the surface of neat PF (Fig. 12c) is naked and there are many pits on the surface. This is due to thermal oxidative decomposition of surface and escape of pyrolysis gas from inside. However, the surface of P-G-S-3 (Fig. 12d) is covered by a large number of irregular objects and undecomposed deep-layer resin. The irregular objects belong to P-G-S-3 which is protected

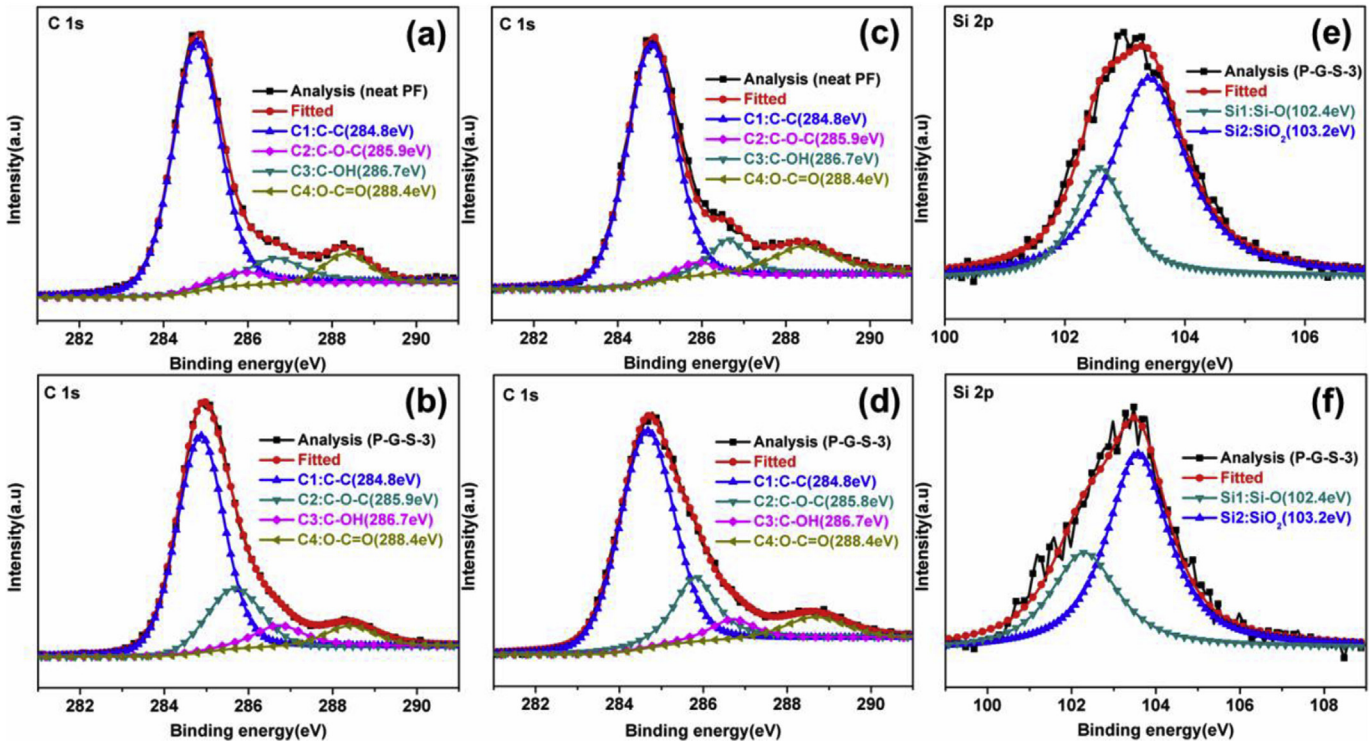


**Fig. 11.** X-ray photoelectron spectra of neat PF and P-G-S-3 in air during thermal oxidative decomposition: (a) (b) C 1s core-spectrum at 550 °C, (c) (d) C 1s core-spectrum at 700 °C, (e) (f) high resolution Si 2p at 550 and 700 °C respectively.

by G-S. After treated at 700 °C, there are many bubbles on the surface and holes in the section part of neat PF (Fig. 13a and b). It should be attributed to fast consumption of thermal oxidative decomposition. And these holes can as a channel for oxygen transport. On the contrary, there are many $SiO_2$ on surface and much less holes in section of P-G-S-3 (Fig. 13c–e). The section of P-G-S-3 expresses skin lamination (shown in Fig. 13f), which is attributed to introduction of G-S. The non-protected resin are consumed but the protected ones are remained by G-S. And $SiO_2$ can as a barrier to protect resin continually from oxidation.

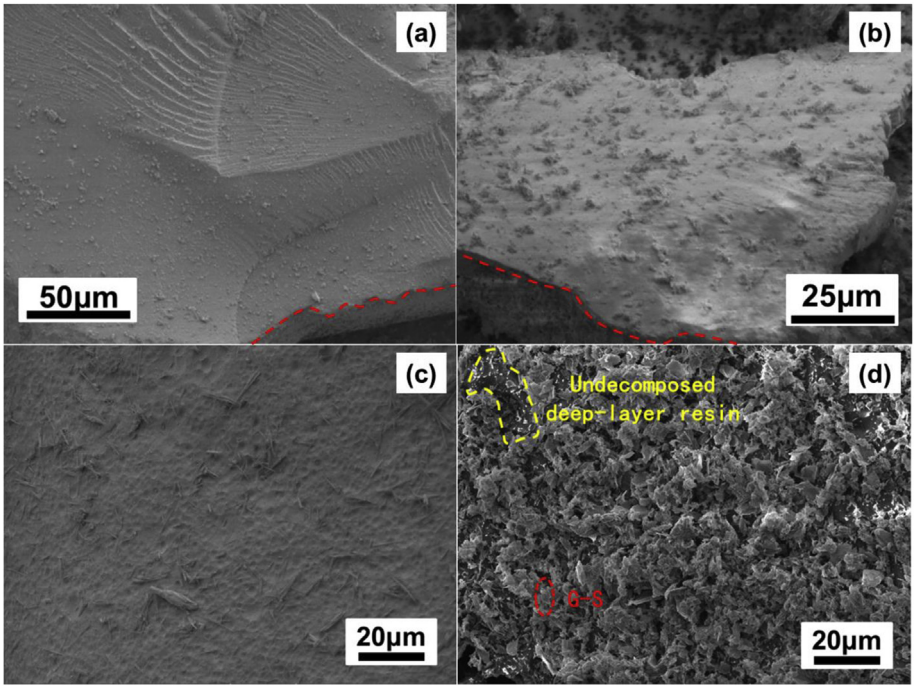


**Fig. 12.** SEM images of neat PF and P-G-S-3 at different temperature treated in air (a) cured neat PF, (b) cured P-G-S-3, (c) neat PF treated at 550 °C, (d) P-G-S-3 treated at 550 °C.

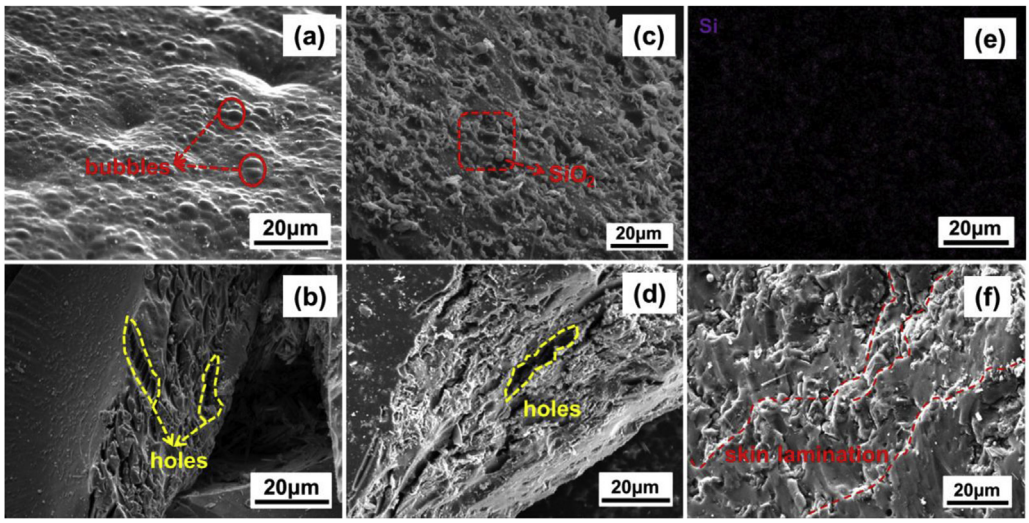


**Fig. 13.** SEM images of neat PF and P-G-S-3 treated at 700 °C in air: (a) and (b) neat PF; (c), (d) and (f) P-G-S-3; (e) Si mapping of image c.

In middle and high temperature range (375–700 °C), the channels which are produced by thermal oxidative decomposition from interior to outside of resin lead to rapid diffusion of oxygen. And adequate contact between resin and oxygen provides the necessary conditions resulting in rapid combustion of resin skeleton structure. However, inner-ring oxygen form of ether bonds of P-G-S-3 has not disappeared at these stages (as shown in Fig. 9c and d and 11b, d), which is the same as in inert atmosphere (in Fig. 8b). This phenomenon shows inadequate contact between the matrix and oxygen. For P-G-S-3 system, G-S as a barrier to prevent or slow down the diffusion rate of oxygen into resin matrix. Less content of oxygen into resin matrix leads to slower rate of thermal oxidative decomposition, and resin matrix can be carbonized rather than complete combustion [32]. Also, the fillers with high aspect ratio, such as nanosheets, can form more continuous thermally conductive network in polymer matrix and are more efficiently in improving the heat transfer to form char layer [33]. Then, stable char layer is not easy to pyrolysis forming oxygen channel, which further improves oxidation resistance. What's more important, $SiO_2$ was loaded on the surface of GR as a shield to protect GR avoiding burning out in such a high temperature environment. This special structure of G-S can give full play to its shielding effect of oxygen in whole process.

Based on the above analysis, we can draw a conclusion that P-G-S-3 has more excellent oxidation resistance in the whole decomposition process (curing, post curing, low, middle and high temperature in oxidative atmosphere).

## 4. Conclusions

In summary, as a kind of functional assistant anti-oxidation filler, G-S was introduced into PF to improve the oxidation resistance.

P-G-S-3 showed excellent oxidation resistance representing the higher residual mass, final decomposition temperature (from about 750 °C up to 900 °C) and the lower thermal oxidative decomposition rate than those of neat PF in oxidative atmosphere. Also, P-G-S-3 expresses higher starting temperature of thermal oxidative decomposition than neat PF.

As the result, when temperature was at 700 °C, the skeleton structure of neat PF had collapsed and only fragments left in structure. However, P-G-S-3 still remained aromatic C-C of skeleton structure, methylene and inner-ring oxygen ether bond as crosslink points in its infrared spectrum by FTIR and XPS. These results provided useful clues for understanding the mechanism of thermal oxidative decomposition and revealed a novel method for improving oxidation resistance of PF.

## Acknowledgments

The authors would like to acknowledge the financial support to this work provided by the National Science Foundation of China (No. 51473134).

## References

[1] Z. Guo, H. Li, Z. Liu, T. Zhao, Preparation, characterization and thermal properties of titanium- and silicon-modified novolac resins, High Perform. Polym. 25 (2013) 42–50.
[2] Y. Zhang, S. Shen, Y. Liu, The effect of titanium incorporation on the thermal stability of phenol-formaldehyde resin and its carbonization microstructure, Polym. Degrad. Stabil. 98 (2013) 514–518.
[3] J. Gao, L. Xia, Y. Liu, Structure of a boron-containing bisphenol-F formaldehyde resin and kinetics of its thermal degradation, Polym. Degrad. Stabil. 83 (2004) 71–77.
[4] S. Wang, X. Jing, Y. Wang, J. Si, High char yield of aryl boron-containing phenolic resins: the effect of phenylboronic acid on the thermal stability and carbonization of phenolic resins, Polym. Degrad. Stabil. 99 (2014) 1–11.
[5] Y. Liu, X. Jing, Pyrolysis and structure of hyperbranched polyborate modified phenolic resins, Carbon 45 (2007) 1965–1971.
[6] C.-L. Chiang, C.-C.M. Ma, Synthesis, characterization, thermal properties and flame retardance of novel phenolic resin/silica nanocomposites, Polym. Degrad. Stabil. 83 (2004) 207–214.
[7] Y. Zhang, S. Lee, M. Yoonessi, K. Liang, C.U. Pittman, Phenolic resin–trisilanolphenyl polyhedral oligomeric silsesquioxane (POSS) hybrid nanocomposites: structure and properties, Polymer 47 (2006) 2984–2996.
[8] C. Liu, K. Li, H. Li, S. Zhang, Y. Zhang, The effect of zirconium incorporation on the thermal stability and carbonized product of phenol–formaldehyde resin, Polym. Degrad. Stabil. 102 (2014) 180–185.
[9] S. Li, Y. Han, F. Chen, Z. Luo, H. Li, T. Zhao, The effect of structure on thermal stability and anti-oxidation mechanism of silicone modified phenolic resin, Polym. Degrad. Stabil. 124 (2016) 68–76.
[10] E.L. Corral, L.S. Walker, Improved ablation resistance of C–C composites using zirconium diboride and boron carbide, J. Eur. Ceram. Soc. 30 (2010) 2357–2364.
[11] Z. Amirsardari, R. Mehdinavaz Aghdam, M. Salavati-Niasari, S. Shakhesi, Enhanced thermal resistance of GO/C/phenolic nanocomposite by introducing ZrB2 nanoparticles, Compos. B Eng. 76 (2015) 174–179.
[12] K.S. Novoselov, Electric field effect in atomically thin carbon films, Science 306 (2004) 666–669.
[13] S. Lijima, Helical microtubules of graphitic carbon, Nature 354 (1991) 56–58.
[14] S. Lijima, T. Ichihashi, Single-shell carbon nanotubes of 1-nm diameter, Nature 363 (1993) 603–605.
[15] A. Noparvar-Qarebagh, H. Roghani-Mamaqani, M. Salami-Kalajahi, Novolac

phenolic resin and graphene aerogel organic-inorganic nanohybrids: high carbon yields by resin modification and its incorporation into aerogel network, Polym. Degrad. Stabil. 124 (2016) 1–14.
[16] A. Mousavi, H. Roghani-Mamaqani, M. Salami-Kalajahi, S. Shahi, A. Abdollahi, Modification of graphene with silica nanoparticles for use in hybrid network formation from epoxy, novolac, and epoxidized novolac resins by sol-gel method: investigation of thermal properties, Express Polym. Lett. 12 (2018) 187–202.
[17] T. Li, S. He, A. Stein, L.F. Francis, F.S. Bates, Synergistic toughening of epoxy modified by graphene and block copolymer micelles, Macromolecules 49 (2016) 9507–9520.
[18] X. Li, Z. Wang, L. Wu, Preparation of a silica nanospheres/graphene oxide hybrid and its application in phenolic foams with improved mechanical strengths, friability and flame retardancy, RSC Adv. 5 (2015) 99907–99913.
[19] T.K. BS, A.B. Nair, B.T. Abraham, P.M.S. Beegum, E.T. Thachil, Microwave exfoliated reduced graphene oxide epoxy nanocomposites for high performance applications, Polymer 55 (2014) 3614–3627.
[20] Z.-J. Wang, D.-J. Kwon, G.-Y. Gu, W.-I. Lee, J.-K. Park, K. Lawrence DeVries, et al., Ablative and mechanical evaluation of CNT/phenolic composites by thermal and microstructural analyses, Compos. B Eng. 60 (2014) 597–602.
[21] J.W. Yu, J. Jung, Y.-M. Choi, J.H. Choi, J. Yu, J.K. Lee, et al., Enhancement of the crosslink density, glass transition temperature, and strength of epoxy resin by using functionalized graphene oxide co-curing agents, Polym. Chem. 7 (2016) 36–43.
[22] K. Yu, M. Wang, K. Qian, X. Lu, J. Sun, The synergy effect of Graphene/SiO2 hybrid materials on reinforcing and toughening epoxy resin, Fibers Polym. 17 (2017) 453–459.
[23] W. Cui, F. Du, J. Zhao, W. Zhang, Y. Yang, X. Xie, et al., Improving thermal conductivity while retaining high electrical resistivity of epoxy composites by incorporating silica-coated multi-walled carbon nanotubes, Carbon 49 (2011) 495–500.
[24] X. Pu, H.-B. Zhang, X. Li, C. Gui, Z.-Z. Yu, Thermally conductive and electrically insulating epoxy nanocomposites with silica-coated graphene, RSC Adv. 4 (2014) 15297–15303.
[25] Y.-T. Xu, Y. Guo, L.-X. Song, K. Zhang, M.M.F. Yuen, X.-Z. Fu, et al., Facile fabrication of reduced graphene oxide encapsulated copper spherical particles with 3D architecture and high oxidation resistance, RSC Adv. 4 (2014) 58005–58010.
[26] R. Wang, D. Zhuo, Z. Weng, L. Wu, X. Cheng, Y. Zhou, et al., A novel nanosilica/graphene oxide hybrid and its flame retarding epoxy resin with simultaneously improved mechanical, thermal conductivity, and dielectric properties, J. Mater. Chem. 3 (2015) 9826–9836.
[27] K. Dongwoo, K. Jee Youn, C. Hyun, S. Jae-Hyoung, H. Hyun Sick, K. Chul Su, et al., Oxidation resistance of iron and copper foils coated with reduced graphene oxide multilayers, 2, ACS Nano 6 (2011) 7763–7769.
[28] B. Chenlu, G. Yuqiang, Y. Bihe, H. Yuan, S. Lei, Functionalized graphene oxide for fire safety applications of polymers: a combination of condensed phase flame retardant strategies, J. Mater. Chem. 22 (2012) 23057–23063.
[29] C.M. Daniela, V.K. Dmitry, M.B. Jacob, S. Alexander, S. Zheng zong, S. Alexander, et al., Improved synthesis of graphene oxide, ACS Nano 4 (2010) 4804–4814.
[30] M.J. William, T.C. Robert, High temperature oxidative degradation of phenol-formaldehyde polycondensates, J. Appl. Polym. Sci. 8 (1964) 2163–2193.
[31] K. Ouchi, Infra-red study of structureal changes during the Pyrolysisi of A Phenol-formaldehyde resin, Carbon 4 (1965) 59–66.
[32] Q. Wu, L.-X. Gong, Y. Li, C.-F. Cao, L.-C. Tang, L. Wu, et al., Efficient flame detection and early warning sensors on combustible materials using hierarchical graphene oxide/silicone coatings, ACS Nano 12 (2017) 416–424.
[33] D. Shen, Z. Zhan, Z. Liu, Y. Cao, L. Zhou, Y. Liu, et al., Enhanced thermal conductivity of epoxy composites filled with silicon carbide nanowires, Sci. Rep. 7 (2017) 2606.